Precision Measurements of Ion-Engine Grids for Erosion Studies

1 August 2000

Prepared by

E. J. BEITING
Space Materials Laboratory
Laboratory Operations

Prepared for

SPACE AND MISSILE SYSTEMS CENTER
AIR FORCE MATERIEL COMMAND
2430 E. El Segundo Boulevard
Los Angeles Air Force Base, CA 90245

Engineering and Technology Group

20010316 131

THE AEROSPACE CORPORATION
CORPORATION
El Segundo, California

Michael Zambrana
SMC/AXE

REPORT DOCUMENTATION PAGE

Public reporting burden for this collection of information is estimated to average 1 hour per response, including the time for reviewing instructions, searching existing data sources, gathering and maintaining the data needed, and completing and reviewing the collection of information. Send comments regarding this burden estimate or any other aspect of this collection of information, including suggestions for reducing this burden to Washington Headquarters Services, Directorate for Information Operations and Reports, 1215 Jefferson Davis Highway, Suite 1204, Arlington, VA 22202-4302, and to the Office of Management and Budget, Paperwork Reduction Project (0704-0188), Washington, DC 20503.

1. AGENCY USE ONLY (Leave blank)	2. REPORT DATE 1 August 2000	3. REPORT TYPE AND DATES COVERED

4. TITLE AND SUBTITLE

Precision Measurements of Ion-Engine Grids for Erosion Studies

5. FUNDING NUMBERS

F04701-93-C-0094

6. AUTHOR(S)

E. J. Beiting

7. PERFORMING ORGANIZATION NAME(S) AND ADDRESS(ES)

The Aerospace Corporation
Laboratory Operations
El Segundo, CA 90245-4691

8. PERFORMING ORGANIZATION REPORT NUMBER

TR-2000(8565)-7

9. SPONSORING/MONITORING AGENCY NAME(S) AND ADDRESS(ES)

Space and Missile Systems Center
Air Force Materiel Command
2430 E. El Segundo Boulevard
Los Angeles Air Force Base, CA 90245

10. SPONSORING/MONITORING AGENCY REPORT NUMBER

SMC-TR-01-04

11. SUPPLEMENTARY NOTES

12a. DISTRIBUTION/AVAILABILITY STATEMENT

Approved for public release; distribution unlimited

12b. DISTRIBUTION CODE

13. ABSTRACT (Maximum 200 words)

Two methods of measuring grid erosion in ion engines and ion-beam sources are described. The first method uses a microscope and mechanical stages to measure four edges on each of two grid holes on a front-back grid pair for a small subset of grid holes. From these measurements, the diameters and roundness of the holes and the intergrid separation and concentricity are derived to a precision of ± 10 µm. The second method uses a digital imaging system and image processing to measure diameter, shape, and area of a large number of holes of a front-back pair of a grid set simultaneously. Square pixels with 21.5 µm sides are recorded using a Kodak 1.6 Megapixel camera and a lens system that images a 20 mm x 30 mm area. Sampling more than 100 holes allows statistical information to be obtained quickly. Standard deviations of hole diameters can be less than the pixel size, but when image processing is required to enhance hole edges due to uneven lighting across the image, a systematic error as large as 10 µm can be introduced.

14. SUBJECT TERMS

Ion engine, Ion-beam source, Grid erosion, Precision mechanical measurement, Satellite propulsion, Electric propulsion diagnostics.

15. NUMBER OF PAGES
22

16. PRICE CODE

17. SECURITY CLASSIFICATION OF REPORT UNCLASSIFIED	18. SECURITY CLASSIFICATION OF THIS PAGE UNCLASSIFIED	19. SECURITY CLASSIFICATION OF ABSTRACT UNCLASSIFIED	20. LIMITATION OF ABSTRACT

NSN 7540-01-280-5500

Acknowledgement

Contents

Figures

Table

1. Introduction

Hall thrusters and gridded ion engines are the two principal satellite electric propulsion systems that use electromagnetic fields for propellant acceleration. In general, gridded ion engines produce higher propellant velocities (specific impulse) than grid-less Hall thrusters. However, grid erosion limits the operational life of ion engines. Accordingly, it is useful to have a diagnostic sensitive enough to measure grid erosion rates after only a few hours of thruster operation. This report describes two techniques developed to measure this grid erosion and documents their capability, accuracy, and operational procedures.

The worldwide electric propulsion community has invested considerable effort in the development of ion engines. Early work on mercury-ion engines led to present-day xenon-ion engines. The most advanced of these are the XIPS thrusters manufactured by Hughes Electronics, which are in routine commercial use. Also, in the United States, NASA developed the 30-cm-dia NSTAR ion engine, which flew on Deep Space 1. Great Britain has developed two flight models: the UK-10 and the larger T-6. Germany has the RIT series and flew the RIT-10 on the EURECA retrievable satellite. The RIT-10, along with the UK-10, are slated to provide North-South stationkeeping on the ARTEMIS satellite. The European Space Agency is developing the ESA-XX that carries components from England, Germany, and Italy. In Japan, MELCO flew the EIS-13 on two satellites, and Toshiba continues to develop a gridded ion engine. The diagnostic methods described in this report are also useful for studying the ion beam sources used for ion milling in the semi-conductor industry. Companies such as Ion Tech, Inc (a division of Veeco) and Commonwealth Scientific Corp. (Alexandria, VA) manufacture both DC and RF gridded ion sources that share the same technology as ion engines.

A typical ion engine has a set of three concentric grids: screen, acceleration (accel), and deceleration (decel) grid, which are either concave or convex. Each of the three grids have the same radius of curvature (which is typically a few tens of centimeters), and each has several thousand holes of equal diameter uniformly distributed over their dished surfaces. The diameter of these holes varies for different models of ion engines but typically it is between 1 and 2 mm. Each hole in the screen grid is nominally aligned with the corresponding holes of the accel and decel grids. This alignment is termed the concentricity. The techniques described below measure the concentricity, size, and shape of these holes as well as the inter-grid separation, thus allowing comparison before and after a burn-in operation. Some ion engines use non-aligned grids to electrostatically vector the beamlets. The methods discussed in this report are equally useful to measure the offsets of these grid sets.

Two instruments were developed. The first comprises a precision mechanical apparatus and a microscope to measure the edges of a small subset of the holes. This apparatus also measures the inter-grid spacing between two adjacent grids. The second device measures properties of hundreds of holes using a high-resolution electronic camera and image processing. Results presented here from the imaging system are the initial attempts at extracting accurate values from the electronic images, and these results should not be interpreted as the ultimate capability of this method.

1

2. Microscopic Method

The apparatus constructed to measure the grid-hole edge positions is shown in Figure 1. The grid-set is mounted on a flange using two screws. The flange is mounted vertically on stacked mechanical drives that permit precision translational and rotational motion. These mechanical drives, in turn, are mounted on an arm connected to a rotation stage whose center of rotation is the center of curvature of the grid-set. A second multi-axis translation stage is mounted on another rotation stage to serve as a positioner for a CCD television camera mated to a microscope objective. This second assembly can be placed on either side of the grid-set.

A subset of holes typically studied lie along three lines that are evenly spaced at intervals of 120°. Each line traverses the center of several dozen holes. Usually, there are about 10 holes measured per line on the screen side and about 10 holes per line measured on the decel side for a total of about 56 holes since the center hole is redundantly measured twice on each side. The three lines are labeled A, B, and C and advance clockwise around the grid-set when viewed from the decel side and counter-clockwise when viewed from the screen side (see Figure 2). Line A has its left end on the decel side.
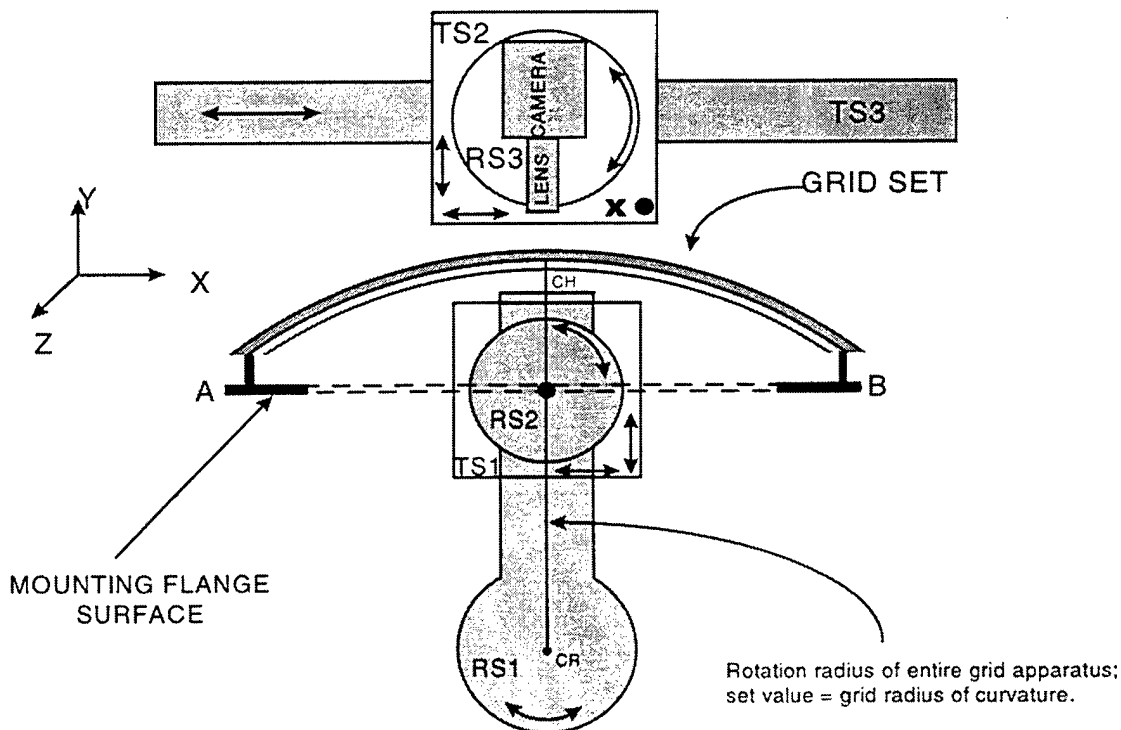

Figure 1. Mechanical setup used to make the microscopic measurements on grid-sets Code: TS = translation stage; RS = rotation stage.
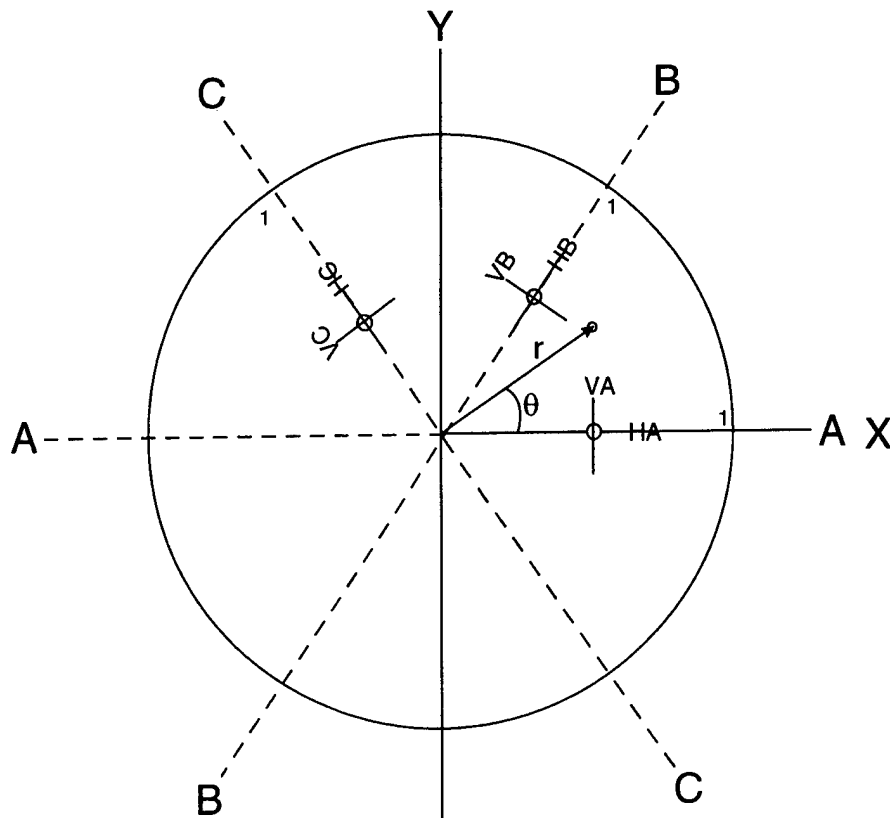
Figure 2. Coordinate system used to define the radial and angular values of the misalignment of the inter-grid holes. The view is on the screen side of the grid-set. The position of the No. 1 hole on each line is indicated.

A measurement sequence starts by rotating the arm holding the grid-set until the hole of interest is in the microscope's field-of-view, then focusing on the outer of the two grids visible, and positioning the microscope cross-hair at the top of the hole. The readout is zeroed and the microscope refocused on the inner surface, and the microscope is translated vertically to the top of the accel hole (position recorded), translated to the bottom of the accel (position recorded), refocused on the outer grid, and translated to the bottom of the outer-hole accel (position recorded). This sequence is repeated for the corresponding four horizontal positions. The measurements are made at the edge of the openings, not at the edge of the bevel on the surface of the grid. By focusing on the outer grid and zeroing the focusing translator readout and then refocusing the image to the accel grid, the distance traveled by the objective is used as a measure of the inter-grid separation. The arm is then rotated to the next hole pair, and the sequence is repeated. The drives used to position the microscope have digital readouts with a precision of 1 μm. The accuracy of the translational measurements (determined empirically) is approximately ± 10 μm.

Typically, the data are presented in three groups of spreadsheet output and plots: the first group shows the data taken before burn-in, the second group shows the data taken after burn-in, and the

4

final group compares these two groups of data. For the first two groups of spreadsheets, there are six sets of spreadsheets and plots, one for each line on each side of the grid-set for both the before and after measurements. Each of the six sets of sheets has a corresponding set of four plots, examples of which are present in Figures 3 and 4. The estimated accuracy of the measurements is indicated by at least one set of error bars per plot. The derived quantities listed on these sheets are the top, bottom, right, and left differences, the horizontal and vertical misalignments (concentricities), the concentricities presented in polar coordinates, the hole diameters, the roundness of the holes measured both as a difference and a ratio, and the inter-grid separation. The definitions of these quantities are given in Appendix 1.

The ROUNDNESS MEASURE graphs show the difference between the horizontal and vertical diameters for both the screen and accel grids and decel and accel grid. These plots would show two straight lines on the abscissa for perfectly round holes. The example plots show that the holes are round to better than 1% for one grid pair, and show excursions as large as 4% from a perfectly round hole for another grid pair.

The inter-grid separation is displayed as a variation from a mean, the plots labeled 1ST SURFACE TO 1ST SURFACE VARIATION, and the plots would be horizontal straight lines for a grid set with constant separation. This measurement of the inter-grid distances was made by focusing the microscope on the outer grid, noting the position of the focusing translator, refocusing the microscope on the inner grid, noting the position, and then taking the difference. The estimated accuracy is ± 20 μm. Although these figures show variation from a mean, absolute differences are presented in reports on specific grid sets.

The alignment of the corresponding holes between the two pairs of grid sets are shown by the plots labeled INTER-GRID HOLE-CENTER MISALIGNMENT and CONCENTRICITY. For both of these plots, all points would lie on the abscissa for perfectly aligned holes. Each of the degrees-of-freedoms of the mechanical setup that could cause such an apparent inter-grid misalignment was examined analytically and empirically. The quantitative analysis of the various misalignments is presented in the Appendix 2.

In order to compare the concentricity among the holes on all three lines, the inter-grid hole misalignments were placeD on the common coordinate system. Figure 2 shows the coordinate system used to calculated the concentricities in polar coordinates. The values of the radial and angular coordinates of the concentricities are listed only on the plotting arrays sheet. An example of this plot is shown in Figure 5. Note that the seemingly large jump in angle from 0° to 350° shown in this plot is only a modest 10° change.

A straightforward method to measure the radius of curvature of the grids is to focus the microscope on the surface of the screen grid at the edge hole, translate the microscope using TS3 in Figure 1 to the center hole, and note the distance required to move the microscope to refocus on the surface. This distance, d, is related to the radius of curvature, R, by $R = (1 - \cos\theta)/d$, where θ is the angle between the center and edge holes. Unfortunately, there is not enough microscope focusing travel available (TS2 shown in Figure 1) to allow this measurement. Thus, a more indirect (and less accurate) method is used to estimate the radius of curvature of the screen grid. This method is described in Appendix 2. The system can be upgraded to the more accurate method if required.
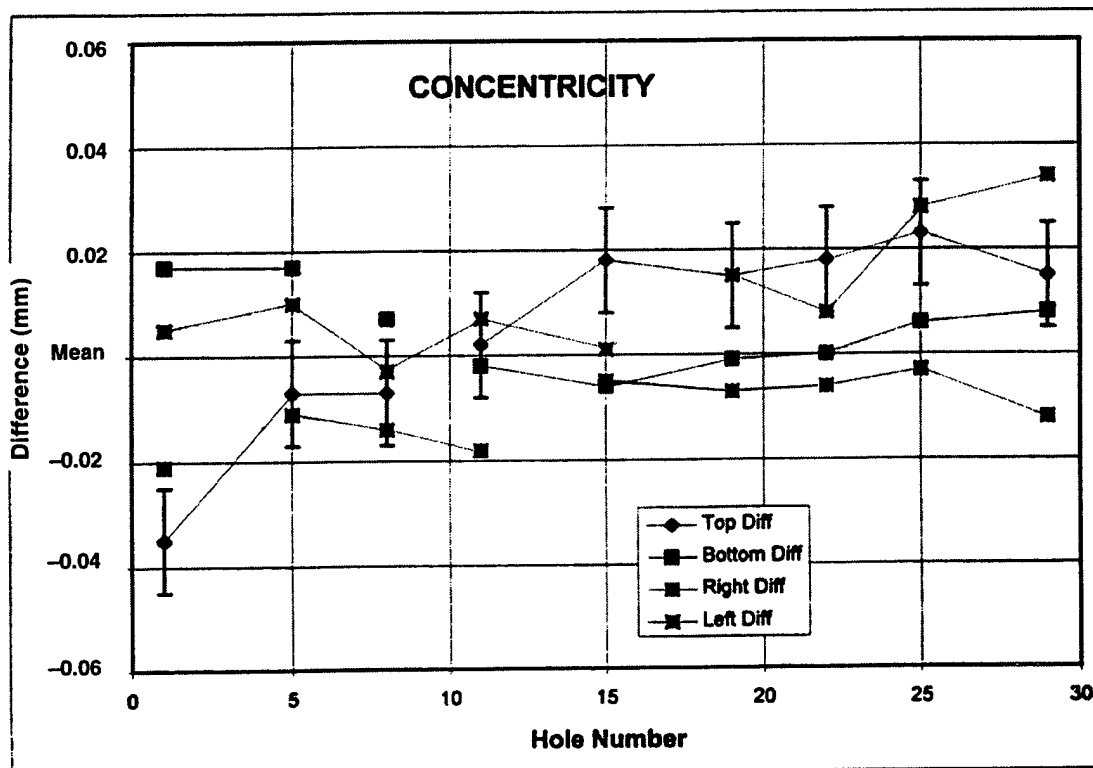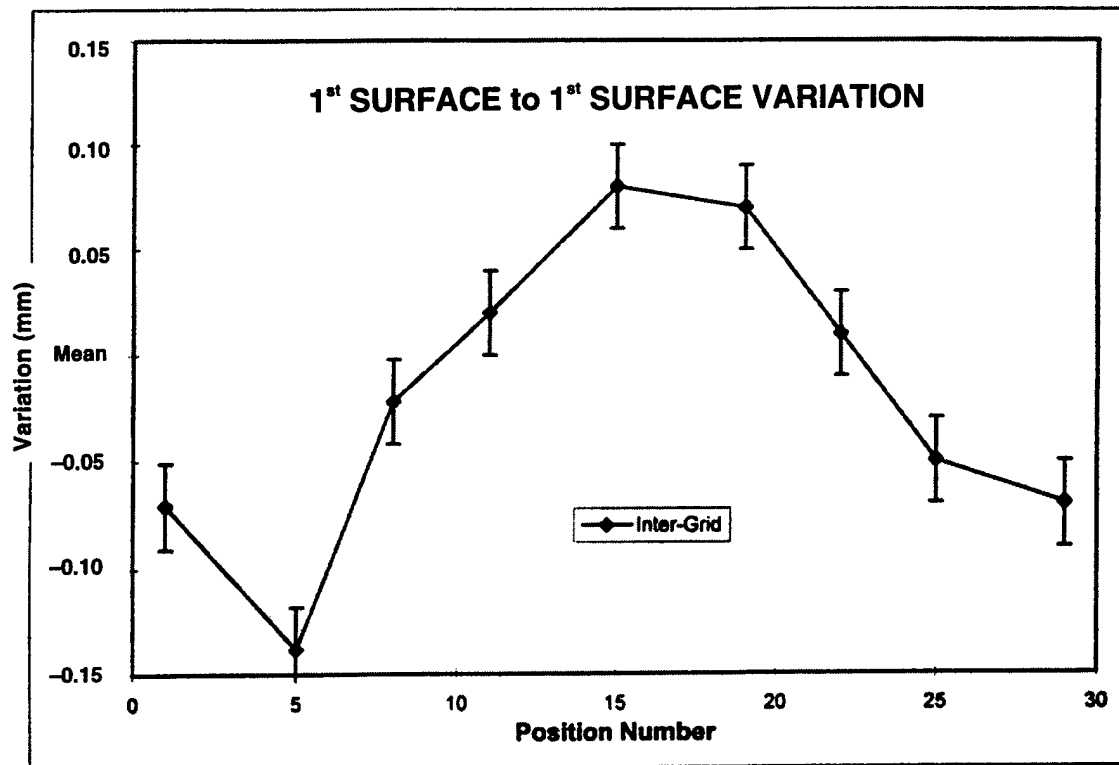
5

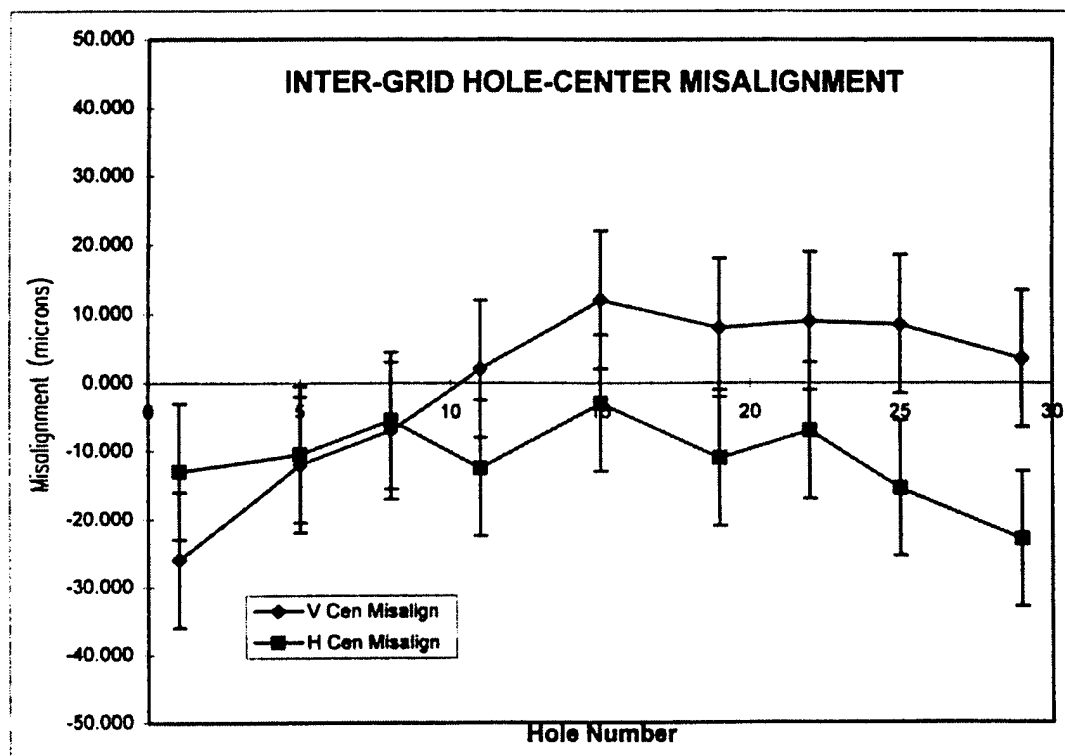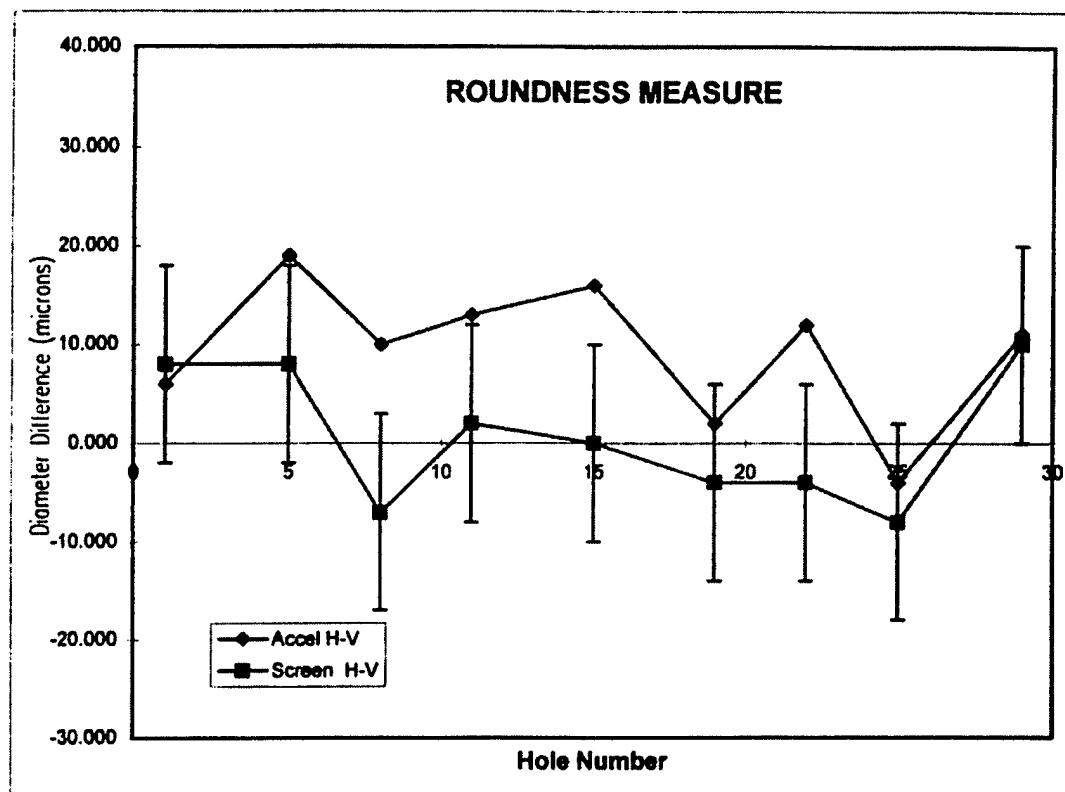Figure 3. Example: Grid separation and concentricity.

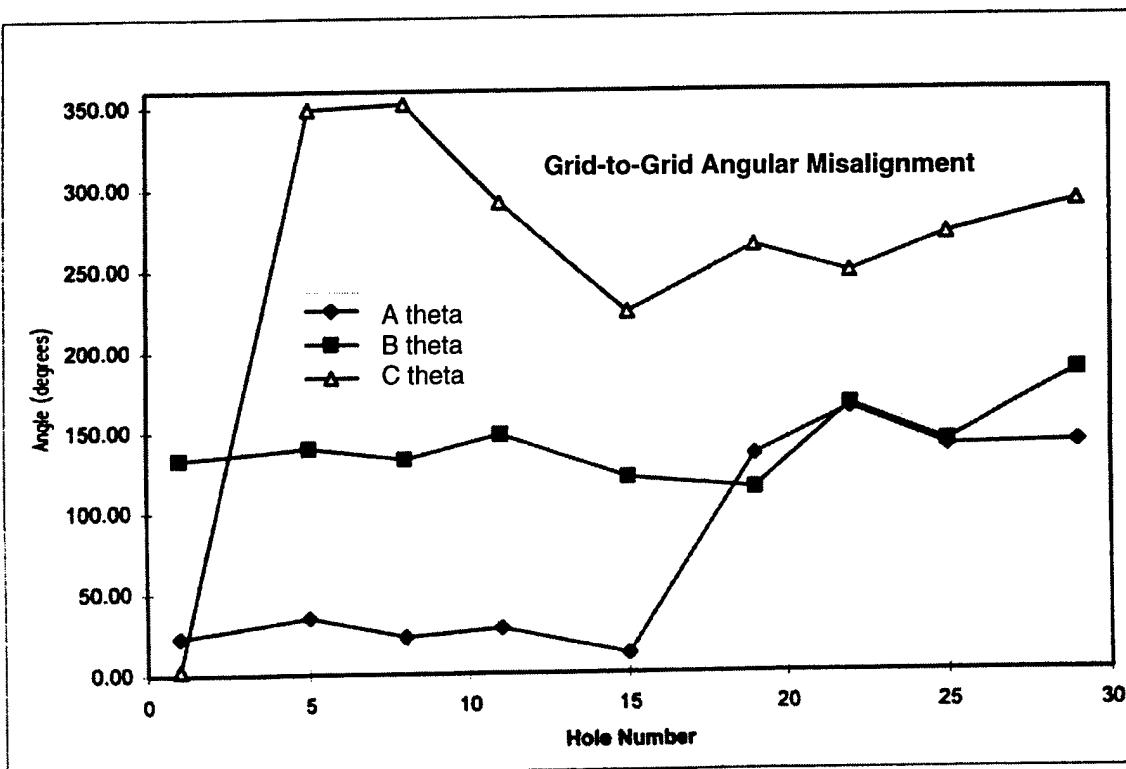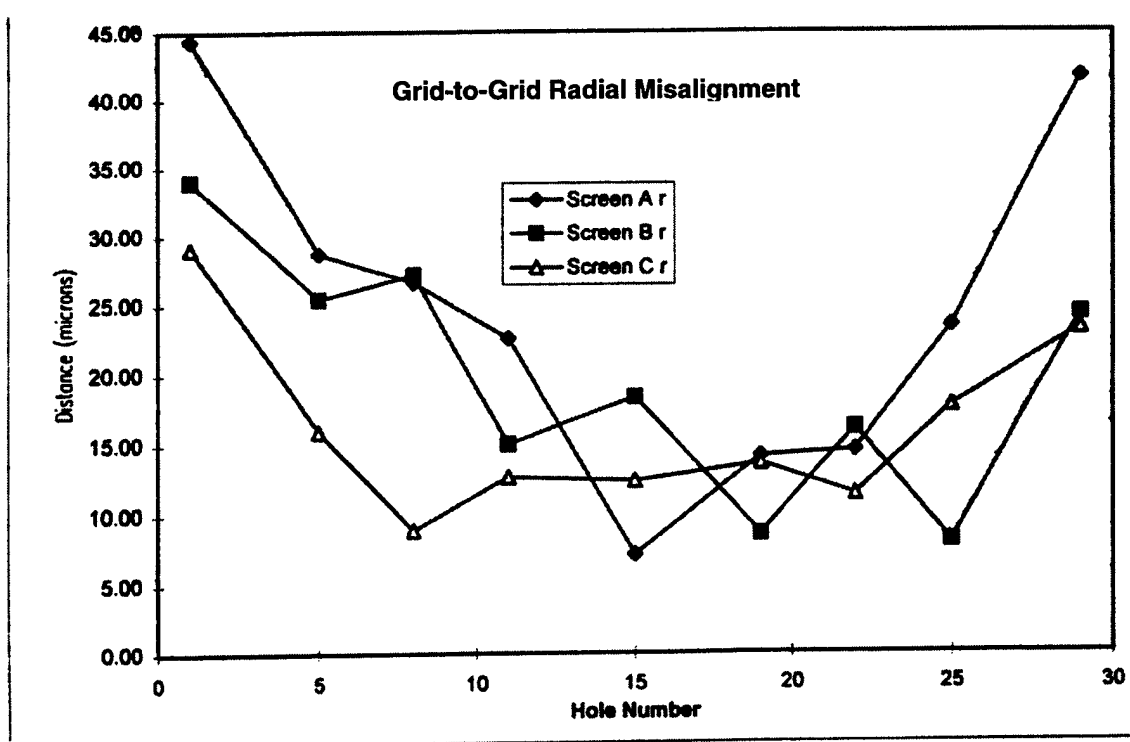Figure 4. Example: roundness and inter-grid hole misalignment.

Figure 5. Example: polar coordinate misalignments.

3. Imaging Method

Statistical information on hole parameters is not available using the microscope setup described in the previous section because only a few holes are measured. Therefore, a method was developed to permit a larger number of holes to be measured simultaneously by electronic imaging. In the examples presented below, a Kodak Megapixel 1.6i CCD electronic camera was used. Characteristics of three different types of exposures are listed in Table 1. The images can be recorded as 8- or 10-bit gray-scale files. An example of an image taken using a 55-mm focal length lens with a 2x lens extender is shown in Figure 6. In this image, each square pixel is 54 μm on a side and does not have the resolution necessary to discern a 1-mil (25-μm) concentricity error.

Table 1. Electronic Image Characteristics

Approx. View	Lens (mm)	Pixel Size (μm)
Entire Grid	55	126
50 mm x 80 mm	2x 55	54
20 mm x 30 mm	2x 105	21.5

Higher resolution images are acquired using a 105-mm focal length lens with a 2x extender lens. An example of an image taken at this resolution is given in Figure 7, where each pixel measures 21.5 μm on a side. These images do have sufficient spatial resolution for quantitative analysis and are analyzed for area, major and minor axis length to an ellipse fit to each hole, and concentricity. In this image, the diameters of 135 screen grid holes were visible. Using a camera with 10 Megapixels and an appropriate lens would increase the number of holes available for analysis in a single exposure to nearly 1000 at this resolution. Of course multiple exposures can be used to increase the number of holes analyzed with this camera.

Example analyses of a high-resolution images are shown in Figures 8 and 9. Although the maximum and minimum diameters of the holes can be listed, the major and minor axes of the ellipses that fit the hole are more reliable indicators of the hole size. The standard deviations are on the order of or less than the pixel size.

Extracting similar numbers from the screen grid where the contrast was not as great between the hole edge and the surrounding border requires image processing. This processing introduces additional variables in the analysis process that can increase the systematic error. Here the standard deviations are greater than the pixel size. The difference between the two sets of values from the same image with different analysis parameters is indicative of a systematic error of about 100 μm. This error is attributed to the spatial filters and contrast adjustments used during the image processing. This processing is sometimes required to acquire the same set of holes acquired during the capture of the accel sizes with the slightly unevenly lit image.

9
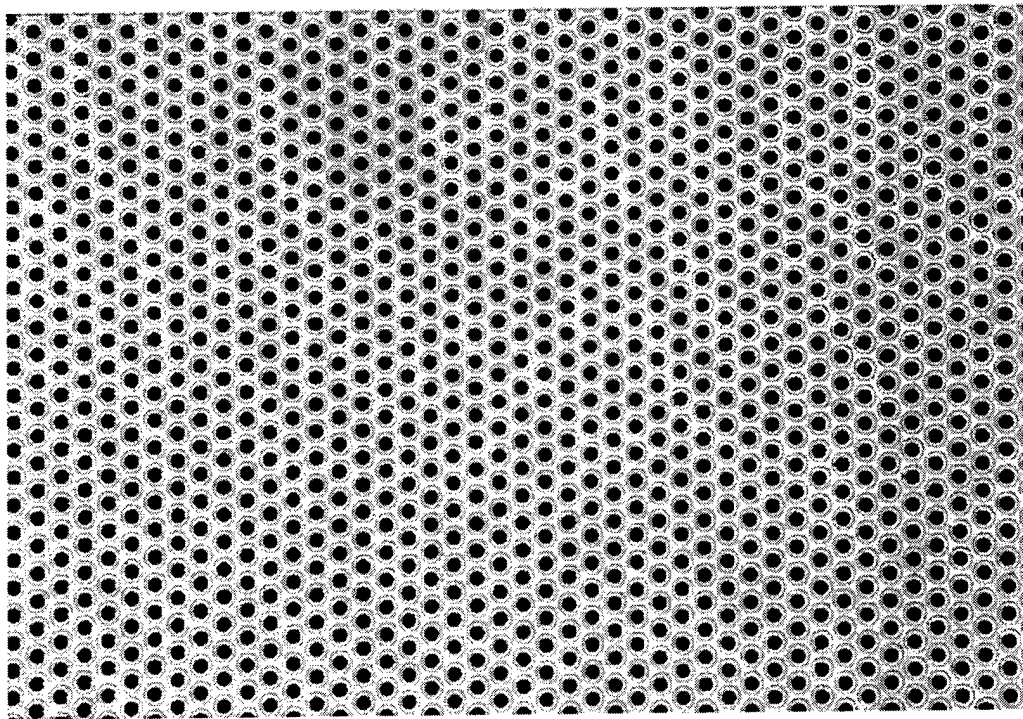
Figure 6.   Image of center of a grid taken with a 2x 55-mm focal length lens. This image contains about 1100 holes and has a pixel size 54 μm.
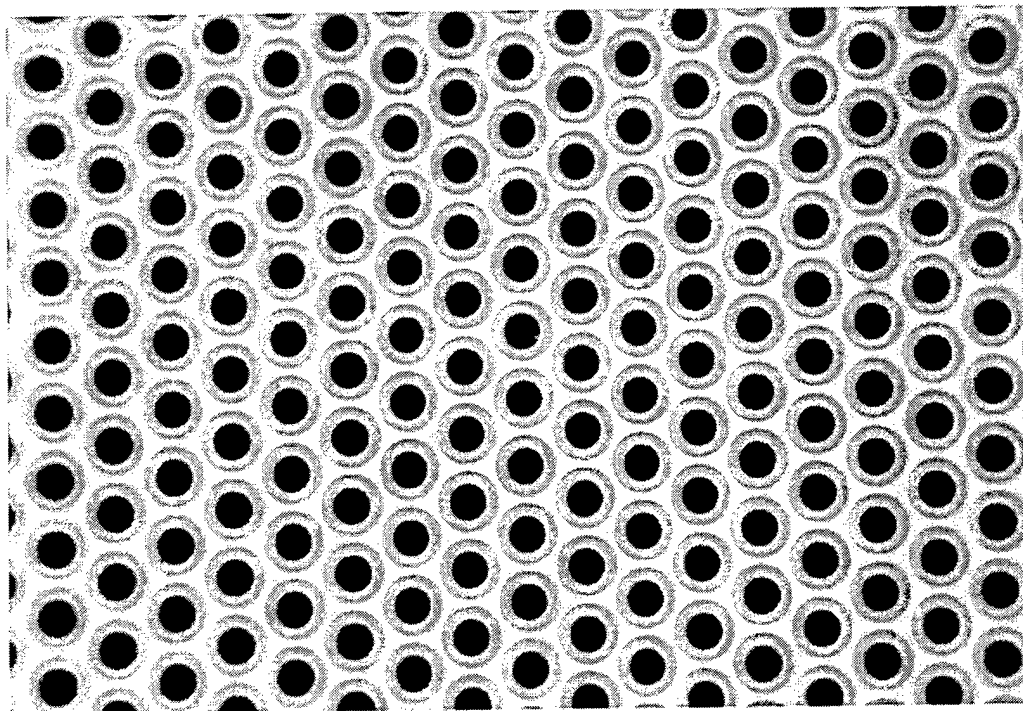

Figure 7.   Central image of screen side of grid-set taken with Kodak Megapixel 1.6i camera through a 2x 105-mm lens. The linear dimension of each pixel is 21.5 μm. No image processing has been performed on this image.

Maj Ax Hist

Maj Ax Hist
0
0
0
0
0
0
0
0
42
59
26
7
1
0
0
0
0
0
0
0
0
0
0
0
0
0

Figure 8. Distribution of hole size for 135 holes.

The area values can be presented and are measured by a direct sum of the pixels in the contrast-differentiated areas used to defined to the hole and are not the areas of the fit ellipses. The maximum and minimum diameters are defined in a similar way and suffer from any artifacts that may cause the perimeters of the holes to be unsmooth.

The concentricity can be measured by taking the difference between the center x and y positions of the corresponding holes of the two grids and calculating a radial distance. De-centering can also be measured using this technique.

If the center of the camera field-of-view is exactly centered on the center hole, one would expect that radial de-centering would increase by the apparent error caused by viewing two concentrically aligned sets of holes projected onto a flat plane. This error is the separation between the grid times the sine of the angle the hole is off the center axis. From center to edge horizontally on the image shown in Figure 7, one would expect an apparent de-centering of about 22 μm. Typical measurements do not show de-centering this large. If the de-centering from one edge to the other edge of an image is not symmetric, the field-of-view of the camera is not centered on the center of the grid.

11

Horizontally along the center line a difference of 4 µm on one side and 10 µm on the other side was measured, indicating that the camera was not exactly centered with the grid center line, and the apparent de-centering is not as large as would be expected with a straightforward geometric calculation. Generally, histograms of images show a standard deviation of less than 10 µm, which is smaller than would be expected for the pixel size and the projection error.
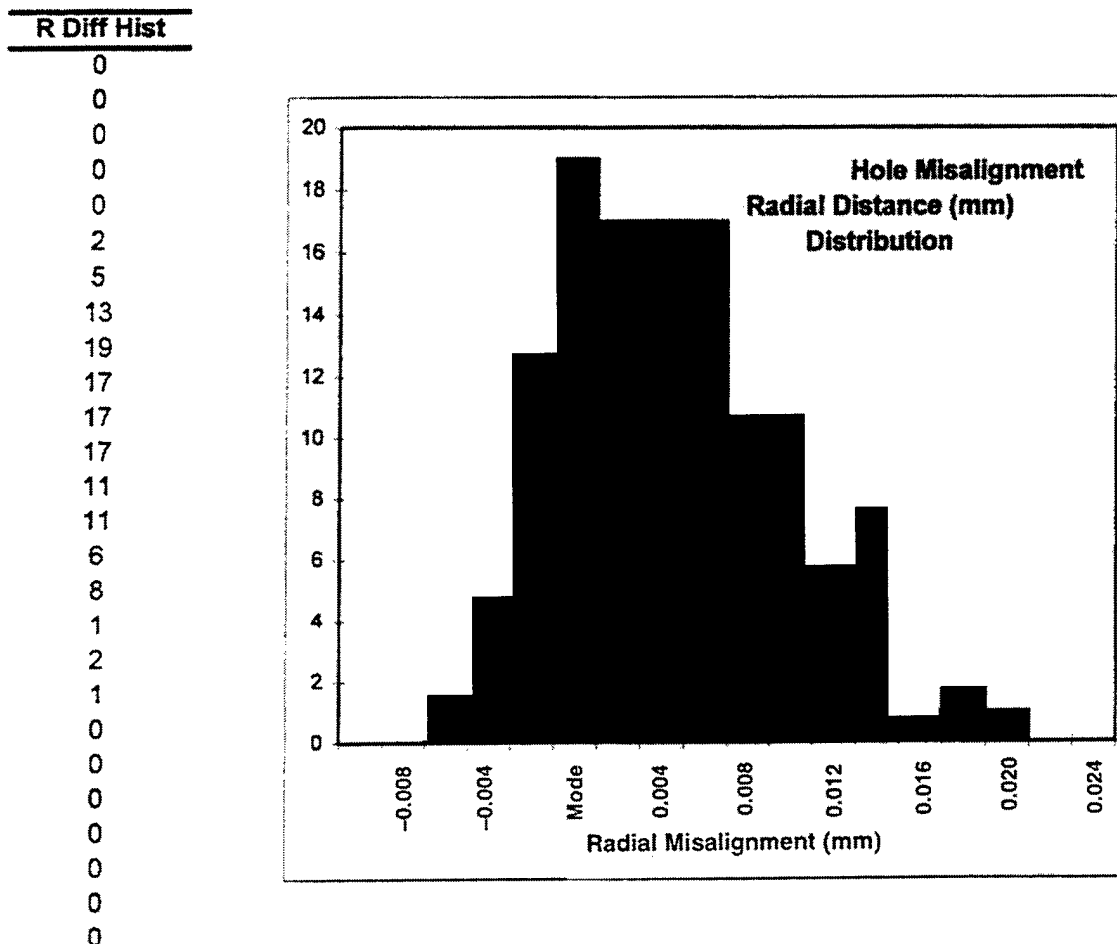
R Diff Hist
0
0
0
0
0
2
5
13
19
17
17
17
11
11
6
8
1
2
1
0
0
0
0
0
0
0

Figure 9. Distribution of hole misalignment for 130 pairs of grid holes.

4. Conclusions

The two methods discussed in this report are complementary. The microscopic method is more accurate but is time intensive and samples only a few holes. The imaging method is much faster and can sample enough holes to produce meaningful statistical information. Both methods require consistent and uniform lighting. The lighting conditions must be identical for both the first (before ion engine operation) and the second (after burn-in operation) measurements or significant errors will be introduced. With good lighting, the imaging method has the potential to achieve better accuracy than the microscopic method if good flat field lenses and high-resolution (>10 Megapixel) CCD cameras are used.

Appendix 1—Definition of Derived Quantities

Information on the Analysis Procedures Used in the Spreadsheets

The order of data acquisition from the digital readout on micrometers and indicators gauges for the Screen Side are:

Screen Top
Accel Top
Accel Bottom
Screen Bottom
Screen Right
Accel Right
Accel Left
Screen Left
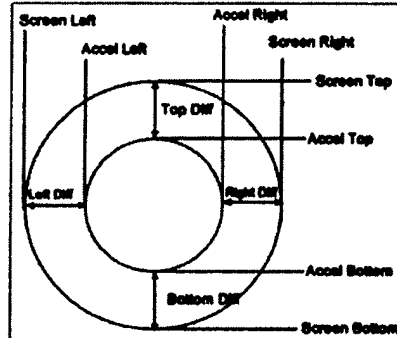
The derived quantities are:

Top Diff = Accel Top - Screen Top = +
Bottom Diff = Screen Bottom - Accel Bottom = +
RightDiff = Accel Right - Screen Right = +
Left Diff = Screen Left - Accel Left = +
V Cen Misalign = (Top Diff - Bottom Diff)/2 = + if center of screen hole is above center of accel hole
H Cen Misalign = (Right Diff- Left Diff)/2 + if center of screen hole is right of center of accel hole

H Accel Dia = Accel Left - Accel Right = +
V Accel Dia = Accel Bottom - Accel Top = +
H Screen Dia = Screen Left - Screen Right = +
V Screen Dia = Screen Bottom - Screen Top = +

Accel H-V = is + if horizontally elongated
Accel H/V = is > 1 if horizontally elongated
Screen H-V = is + if horizontally elongated
Screen H/V = is > 1 if horizontally elongated

Misalign r = distance of screen hole center to accel hole center mismatch
theta = angle of screen hole center to accel hole center mismatch referenced to line A with hole 1 in positive direction

15

Appendix 2—Sensitivity Analysis of Mechanical Misalignment

The setup used to make the microscopic studies of the grid-set has a number of degrees-of-freedom. Misalignment of several of these degrees-of-freedom can manifest themselves as apparent inaccuracies in the manufacture of the grid-set. Accordingly, the effects of these errors in alignment were studied quantitatively, and the results are included here as a set of figures and Mathcad sheets. The alignment procedure and a listing of the degrees-of-freedom are included in Appendix 3.

A mismatch between the radius of rotation used to rotate the grid set into the field-of-view of the microscope with the radius of the grid-set will manifest itself as a defocusing of the image as the grid-set is rotated from center to edge. This mismatch also can cause an apparent misalignment of the centers of the corresponding holes in the adjacent grids. The defocus is shown by δ, and apparent misalignment is shown by ϵ in Figure 1-1. When the radius of curvature was set up to be 20 in., a center-to-edge defocus ($\theta = 0.108$ rad) was measured to be about 100 μm ± 20 μm. Manually changing the rotational radius by 3 mm changed the defocus 35 μm ± 20 μm. The equation at the top of the first Mathcad page is derived by applying the sine and cosine laws to the triangle shown in Figure 1-1. Solving this equation for radial mismatch and plotting as a function of defocus on this sheet indicates a radial mismatch of about 18 mm for the 100 μm defocus, or that the radius of curvature of the grid is $20 \times 25.4 - 18 = 490$ mm. The next sheet displays the apparent inter-grid hole misalignment as a function of defocus and as a function of angle for a 0.5-in. radial mismatch. This mismatch causes less than 0.2 μm de-centering and is clearly not the cause mismatch measured.
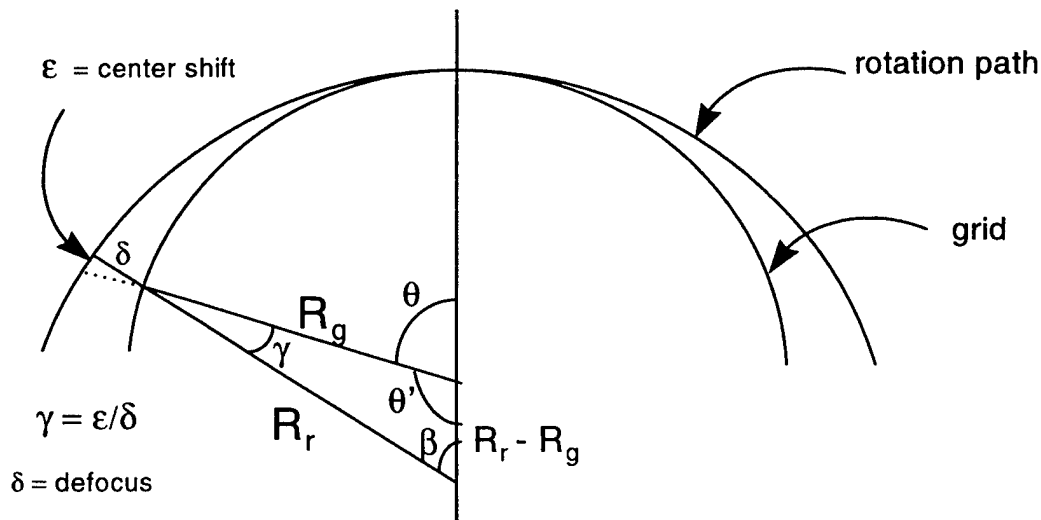

Figure 1-1.   Geometry used to calculate the effect of a mismatch between the radius of rotation and the radius of curvature on the screen grid.

The next sheets investigate the effect of an off center ring rotation on the grid hole concentricity. These relevant variables are shown in Figure 1-2. These calculations indicate that a 1° misalignment in the of the rotational system with respect to the grid-set will result in a 13-μm de-centering at the edge of the grid-set in the horizontal direction only and direction of the de-centering does not change from one side of the grid-set to the other. The alignment of the test configuration is believed to be better than 1°, and the edge de-centering tends to be 2 to 3 times this value.
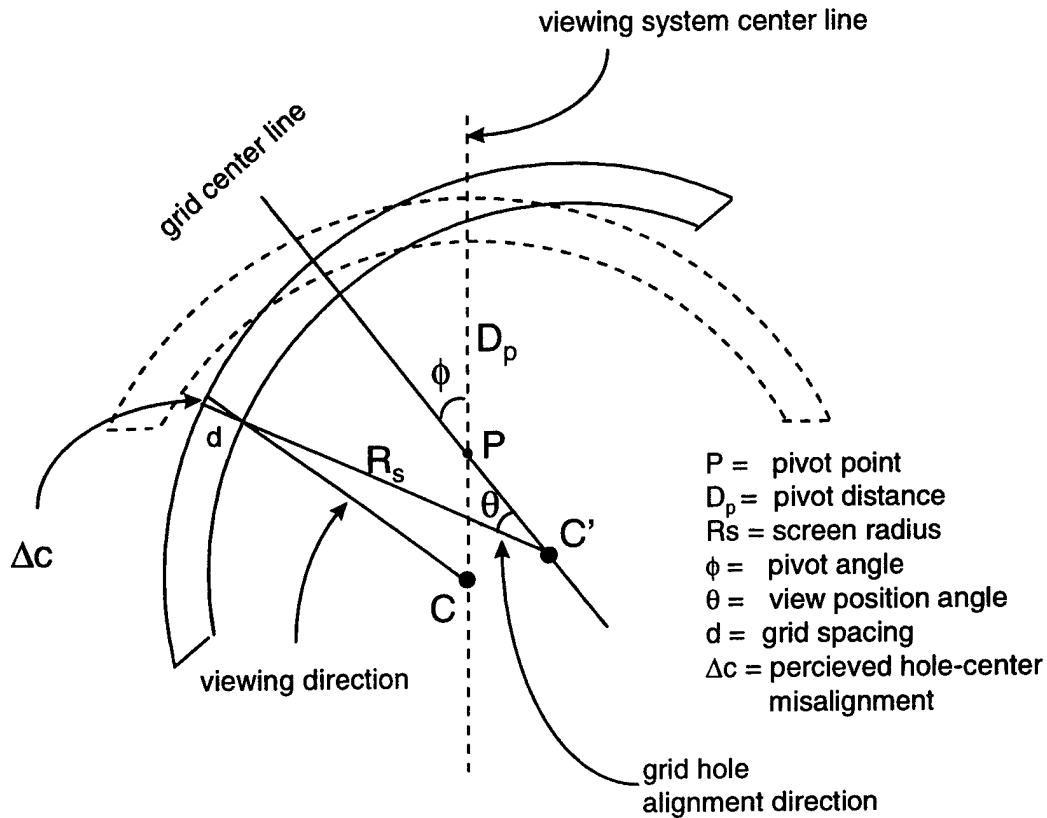

P = pivot point
D_p = pivot distance
Rs = screen radius
φ = pivot angle
θ = view position angle
d = grid spacing
Δc = percieved hole-center
misalignment

Figure 1-2. Effect of the a misaligned center of rotation.

Sensitivity to Grid Radius-Rotational Radius Mismatch Master Equation:

$$\left(\frac{Rr - Rg}{Rg} - \cos(\pi - \theta)\right)\left[\left(\frac{Rg}{Rr - \delta}\right)\cdot\sin(\pi - \theta)\right] - \sin(\pi - \theta)\cdot\left[\frac{Rg^2 - (Rr - \delta)^2 - (Rr - Rg)^2}{-2\cdot(Rr - \delta)\cdot(Rr - Rg)}\right]$$

Solve for δ:

$$\delta f(Rr, Rg, \theta) := Rr - \frac{1}{2}\cdot\sqrt{4\cdot Rr^2 - 8\cdot Rr\cdot Rg + 8\cdot Rg^2 + 8\cdot\cos(\theta)\cdot Rg\cdot Rr - 8\cdot\cos(\theta)\cdot Rg^2}$$

Solve for Rr where Rr is the radius of rotation, and θ is the angle of rotation:

$$Rrf(\delta, \theta, Rg) := \frac{1}{2}\cdot\frac{\left(-2\cdot Rg^2 + 2\cdot\cos(\theta)\cdot Rg^2 + \delta^2\right)}{(-Rg + \cos(\theta)\cdot Rg + \delta)}$$
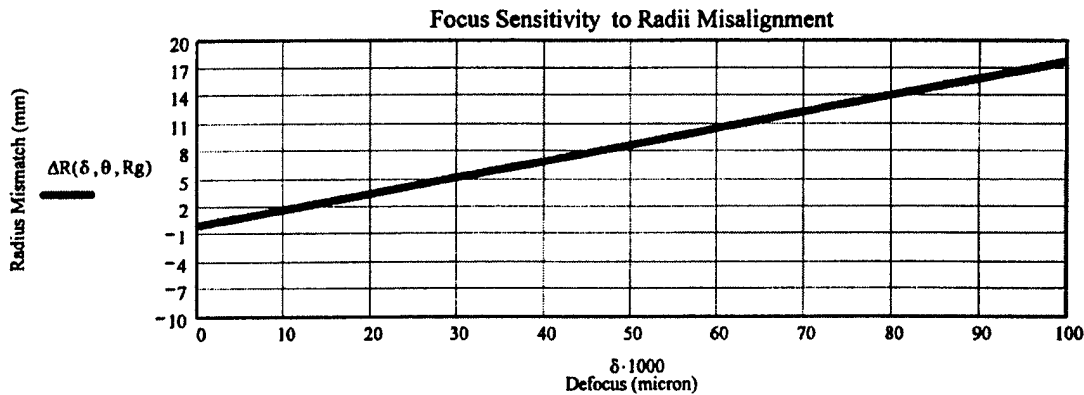
$$\Delta R(\delta, \theta, Rg) := Rrf(\delta, \theta, Rg) - Rg$$

$Rg := 25.4\cdot20$ Grid radius of curvative in mm

$\theta := 0.108$ radians

$\delta := 0.0, 0.01 .. 0.1$ in mm $\Delta R(0.1, 0.108, 20\cdot25.4) = 17.762$

Focus Sensitivity to Radii Misalignment

$\theta := 0.01, 0.02 .. 0.11$ $Rr := 20.5\cdot25.4$ $Rg := 20\cdot25.4$ **For 0.5 inch Mismatch**

Focus Sensitivity to Angle

19
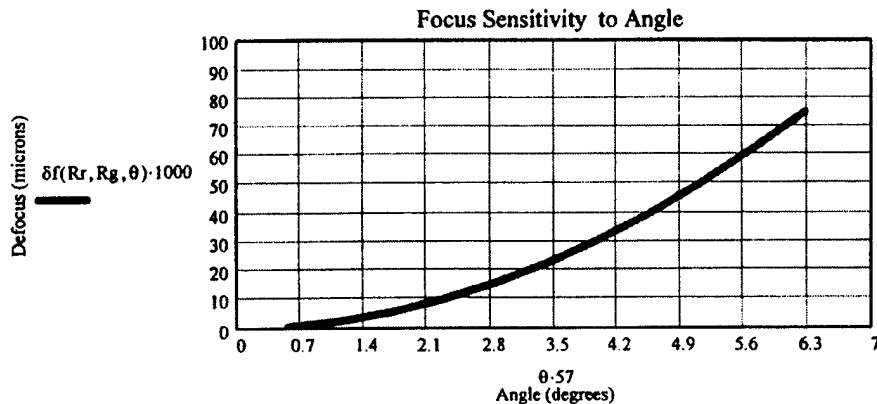
$\theta := 0.108$ radians

$\delta := 0.0, 0.01 .. 0.2$ in mm

$$\varepsilon(\delta,\theta,Rg) := \delta \cdot asin\left(\frac{Rrf(\delta,\theta,Rg) - Rg}{Rrf(\delta,\theta,Rg) - \delta}\right) \cdot sin(\theta)$$

Grid Holes Misalignment vs Defocus
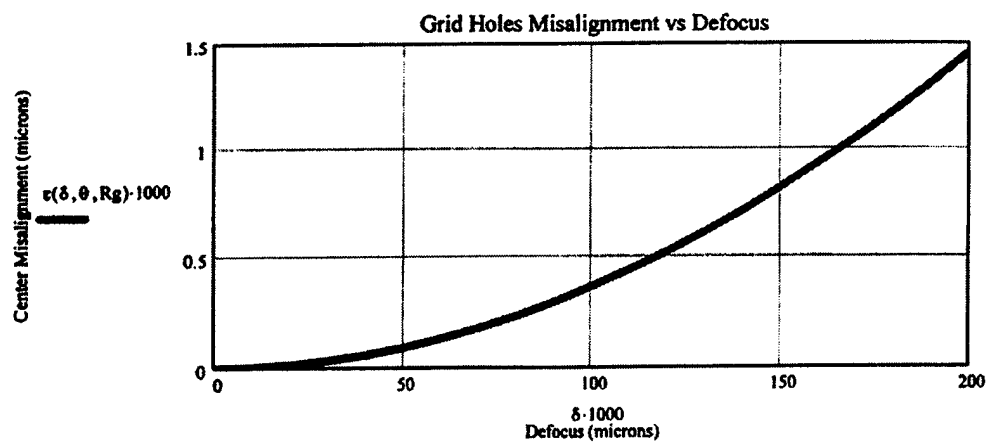
Grid Hole Misalignment as a Function of Defocus at Edge

$$\varepsilon(Rr,Rg,\theta) := \delta f(Rr,Rg,\theta) \cdot asin\left(\frac{Rrf(\delta f(Rr,Rg,\theta),\theta,Rg) - Rg}{Rrf(\delta,\theta,Rg) - \delta f(Rr,Rg,\theta)}\right) \cdot sin(\theta)$$

$\theta := -0.108, -0.1079 .. 0.108$
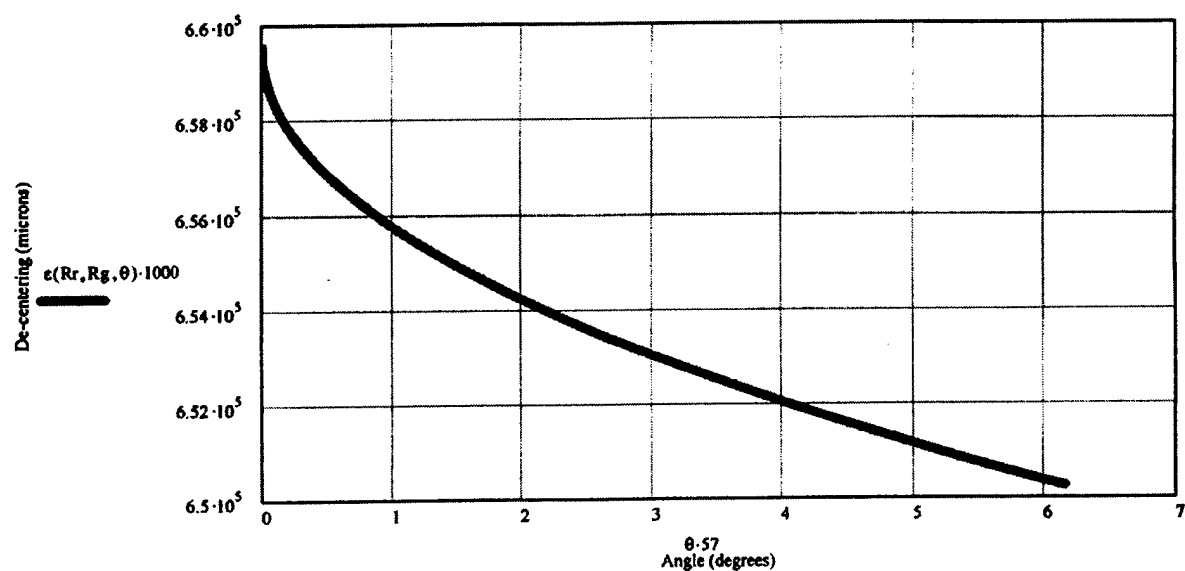
Sensitivity of Off-Center Ring Rotation on Grid Hole Concentricity

$Rs := 20 \cdot 25.4$

$Dp := 80$

$\theta := 0.108$ Lengths in mm, angles in radians

$d := 0.860$

$\alpha(\phi) := \pi - (\theta + \phi)$

$b(\phi) := (Rs - Dp) \cdot \dfrac{\sin(\theta)}{\sin(\alpha(\phi))}$

$g(\phi) := (Rs - Dp) \cdot \dfrac{\sin(\phi)}{\sin(\alpha(\phi))}$

$a(\phi) := Rs - Dp - b(\phi)$

$f(\phi) := Rs - g(\phi)$

$h(\phi) := \sqrt{f(\phi)^2 + a(\phi)^2 - 2 \cdot a(\phi) \cdot f(\phi) \cdot \cos(\alpha(\phi))}$

$\psi(\phi) := \operatorname{asin}\left(\dfrac{a(\phi)}{h(\phi)} \cdot \sin(\alpha(\phi))\right)$

$\Delta c(\phi) := d \cdot \tan(\psi(\phi))$

$\phi := 0.001, 0.002 .. 0.1$ $\Delta c(0.0175) = 0.013$

Grid Pivot Misalignment

(y-axis) Grid Holes Misalignment — $\Delta c(\phi) \cdot 1000$

(x-axis) $\phi \cdot 57$ Pivot Angle

$$\psi(Rs,Dp,\theta,\phi) := asin\left[\frac{\left[Rs - Dp - (Rs - Dp)\cdot\dfrac{\sin(\theta)}{\sin(\theta + \phi)}\right]}{\sqrt{\begin{array}{l}\left[Rs - (Rs - Dp)\cdot\dfrac{\sin(\phi)}{\sin(\theta + \phi)}\right]^2 + \left[Rs - Dp - (Rs - Dp)\cdot\dfrac{\sin(\theta)}{\sin(\theta + \phi)}\right]^2 \cdots \\ + 2\cdot\left[Rs - Dp - (Rs - Dp)\cdot\dfrac{\sin(\theta)}{\sin(\theta + \phi)}\right]\cdot\left[Rs - (Rs - Dp)\cdot\dfrac{\sin(\phi)}{\sin(\theta + \phi)}\right]\cdot\cos(\theta + \phi)\end{array}}}\right]\cdot\sin(\theta + \phi)$$

$$\Delta c(Rs,Dp,\theta,\phi,d) := d\cdot\tan(\psi(Rs,Dp,\theta,\phi))$$

$Rs := 20\cdot 25.4$

$Dp := 80$ **Lengths in mm, angles in radians**

$\theta := 0.108$

$\phi := 0.0175$

$d := 1.0$

$$\Delta c(Rs,Dp,\theta,\phi,d)\cdot 1000 = 14.702 \quad \text{micron}$$

$$\phi := 0.001, 0.002 .. 0.1$$

Grid Pivot Misalignment

Center Misalignment (microns)

$\Delta c(Rs,Dp,\theta,\phi,d)\cdot 1000$

$\phi \cdot 57$
Pivot Angle (degrees)
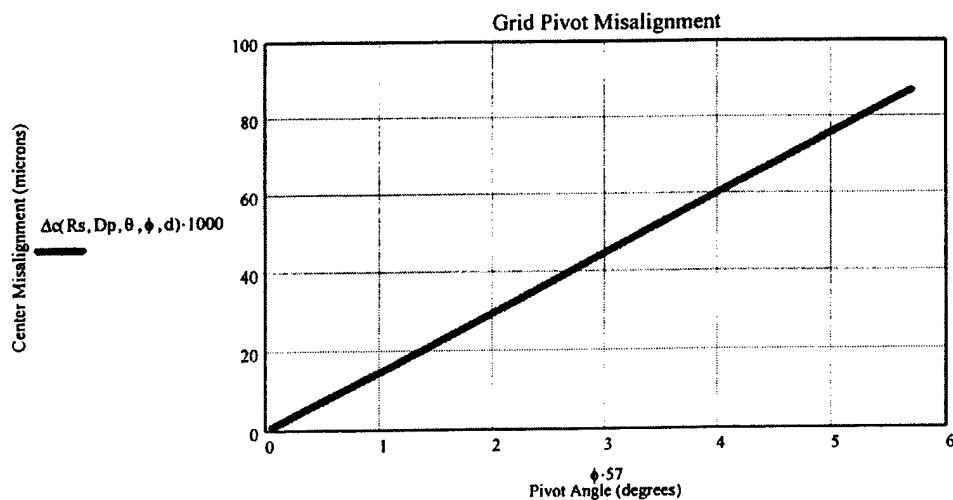
Appendix 3—Alignment Procedure for Ion Engine Grid Set

(All symbols are those shown in Figure 1)
With grid **not** installed on mounting flange:

1. Set mounting flange holes level using digital level and long screws by shimming the base of the flange.

2. Set distance <u>CR-CH</u> equal to approximately the radius of grid set (20 ± 0.5') using TS1-Y.

3. Set mounting fixture center on centerline of rotation arm with TS1-X using two-point sighting fixture and long ruler.

4. Set mounting fixture surface (grid cord AB) perpendicular to the centerline of rotation arm using large dial indicator centered over centerline of rotation arm.

5. Level camera bracket in both directions (shim for y direction as required).

6. Adjust camera perpendicular to its mount.

7. Set camera parallel to the centerline of the rotation arm using a right-angle block between rail and large traverse TS4-X . Note: this assumes that all mounts holding camera are square.

Install grid.

8. With the centerline of rotation arm perpendicular to the camera, use large translator TS3-X to center on grid center hole CH.

9. Check that grid holes along measurement row do not move vertically excessively as rotation arm is rotated through entire grid. Adjust by rotating grid in mounting fixture screws.

10. Set grid radius of curvature to radius of rotation by finding center hole of grid and adjusting TS1-Y so that the grid remains in focus when RS1 is rotated from edge to center to edge of grid. (100 µm defocus = 12 mm radii mismatch.)

<u>Degrees of freedom that must be set:</u>

1. TS1-X (Sensitivity considered in #3 below; should change sign for arm rotation.)

2. TS1-Y (Sensitivity calculated for radial mismatch, changes sign for arm rotation.)

3. RS2 (Sensitivity calculated; does not change sign for arm rotation)

4. RS3 (Sensitivity not considered, should not change sign with arm rotation.)

5. Camera rotation about horizontal axis. (Should be same as #4.)

6. TS3 (Sensitivity not considered, should not change sign with arm rotation.)

Translation stage TS2 is used to make the measurements and is not used for alignment.

LABORATORY OPERATIONS

The Aerospace Corporation functions as an "architect-engineer" for national security programs, specializing in advanced military space systems. The Corporation's Laboratory Operations supports the effective and timely development and operation of national security systems through scientific research and the application of advanced technology. Vital to the success of the Corporation is the technical staff's wide-ranging expertise and its ability to stay abreast of new technological developments and program support issues associated with rapidly evolving space systems. Contributing capabilities are provided by these individual organizations:

Electronics and Photonics Laboratory: Microelectronics, VLSI reliability, failure analysis, solid-state device physics, compound semiconductors, radiation effects, infrared and CCD detector devices, data storage and display technologies; lasers and electro-optics, solid state laser design, micro-optics, optical communications, and fiber optic sensors; atomic frequency standards, applied laser spectroscopy, laser chemistry, atmospheric propagation and beam control, LIDAR/LADAR remote sensing; solar cell and array testing and evaluation, battery electrochemistry, battery testing and evaluation.

Space Materials Laboratory: Evaluation and characterizations of new materials and processing techniques: metals, alloys, ceramics, polymers, thin films, and composites; development of advanced deposition processes; nondestructive evaluation, component failure analysis and reliability; structural mechanics, fracture mechanics, and stress corrosion; analysis and evaluation of materials at cryogenic and elevated temperatures; launch vehicle fluid mechanics, heat transfer and flight dynamics; aerothermodynamics; chemical and electric propulsion; environmental chemistry; combustion processes; space environment effects on materials, hardening and vulnerability assessment; contamination, thermal and structural control; lubrication and surface phenomena.

Space Science Application Laboratory: Magnetospheric, auroral and cosmic ray physics, wave-particle interactions, magnetospheric plasma waves; atmospheric and ionospheric physics, density and composition of the upper atmosphere, remote sensing using atmospheric radiation; solar physics, infrared astronomy, infrared signature analysis; infrared surveillance, imaging, remote sensing, and hyperspectral imaging; effects of solar activity, magnetic storms and nuclear explosions on the Earth's atmosphere, ionosphere and magnetosphere; effects of electromagnetic and particulate radiations on space systems; space instrumentation, design fabrication and test; environmental chemistry, trace detection; atmospheric chemical reactions, atmospheric optics, light scattering, state-specific chemical reactions and radiative signatures of missile plumes.

Center for Microtechnology: Microelectromechanical systems (MEMS) for space applications; assessment of microtechnology space applications; laser micromachining; laser-surface physical and chemical interactions; micropropulsion; micro- and nanosatellite mission analysis; intelligent microinstruments for monitoring space and launch system environments.

Office of Spectral Applications: Multispectral and hyperspectral sensor development; data analysis and algorithm development; applications of multispectral and hyperspectral imagery to defense, civil space, commercial, and environmental missions.